Long-term in vivo single cell tracking reveals the switch of migration patterns in adult-born juxtaglomerular cells of the mouse olfactory bulb

Yajie Liang[1], Kaizhen Li[1], Kristoffer Riecken[2], Anatoliy Maslyukov[1], Diego Gomez-Nicola[3], Yury Kovalchuk[1], Boris Fehse[2] & Olga Garaschuk[1]

[1]Institute of Physiology II, University of Tübingen, 72074 Tübingen, Germany

[2]Research Dept. Cell and Gene Therapy, University Medical Center Hamburg-Eppendorf, 20246 Hamburg, Germany

[3]Centre for Biological Sciences, University of Southampton, SO166YD Southampton, United Kingdom

Running title:

Neural stem cells switch migration patterns in the OB

Correspondence should be addressed to:

Prof. Dr. Olga Garaschuk

Institute of Physiology II, University of Tübingen

Keplerstr. 15, 72074 Tübingen, Germany

Tel: +49-07071 29 73640

Fax: +49-07071 29 5395

E-mail: olga.garaschuk@uni-tuebingen.de

Abstract

The behavior of adult stem cells can be easily monitored in cell culture or lower model organisms, but longitudinal observation of individual mammalian stem cells in their native microenvironment still proves to be a challenge. Here we have established an approach named optical cell positioning system for long-term in vivo single cell tracking, which integrates red-green-blue cell labeling with repeated angiography. By combining this approach with in vivo two-photon imaging technique, we characterized the in vivo migration patterns of adult-born neurons in the olfactory bulb. In contrast to the traditional view of mere radial migration of adult-born cells within the bulb, we found that juxtaglomerular cells switch from radial to long distance lateral migration upon arrival at their destination layer. This unique long distance lateral migration has characteristic temporal (stop-and-go) and spatial (migratory, uni- or multidirectional) patterns, with clear cell age-dependent decrease in the migration speed. The active migration of adult-born cells coincides with the time period of initial fate determination and is likely to impact on the integration sites of adult stem cells, their odor-responsiveness as well as their survival rate.

Keywords:

Adult neurogenesis; migration; single cell tracking; RGB marking; two-photon microscopy.

Introduction

It has been more than two decades since the discovery of the long distance migration of mammalian adult-born neural stem cells from the subventricular zone (SVZ) to the olfactory bulb (OB) through the rostral migratory stream (RMS) [1, 2]. Dividing neuroblasts undergo tangential migration in the RMS, and then radial migration up into the OB, where they differentiate into two groups of functional interneurons: granule cells (GCs) and juxtaglomerular neurons (JGNs) [3-10]. Whereas the dynamics of SVZ cell migration as well as the tangential migration of neuroblasts in, and their detachment from the RMS have been studied in much detail [10-16], little is known about their migratory behavior within the olfactory bulb.

Most studies of the migratory behavior of adult-born cells within the OB used immunohistochemistry providing only static views of this dynamic process [17, 18]. Monitoring migration of eGFP-positive neuroblasts in acute brain slices of adult and juvenile mice, Nam et al. [15] have shown that in contrast to the SVZ and caudal RMS, where the majority of neuroblasts were migratory, more rostral neuroblasts slowed or stopped at the edge of the RMS. They concluded that “migration is minimal when cells reach the periglomerular layer of the olfactory bulb”. In an elegant in vivo study Mizrahi [19] described the dynamic changes of dendrite morphology in adult born cells, and hypothesized that adult born JGNs may migrate along the glomerular layer, but could not test his hypothesis due to the lack of a robust approach for single cell tracking. In our previous work, we also observed a displacement of cell bodies of JGNs during a 4-hour-long observation time window (e.g. Fig. 2a in ref. [20]), but were unable to perform long-term single cell tracking in conditions of an acute experiment.

There are mainly two challenges for long-term single cell tracking in the OB: one is how to mark individual cells with unique tags, the other being the lack of a stable landmark which could be visualized repetitively in a convenient way.

In this study, we have overcome these obstacles by introducing a new approach, “optical cell positioning system” (oCPS), allowing an accurate monitoring of the position of many individual cells over days and weeks of their migration within the OB. In contrast to what was assumed previously (see above), the long-term single cell tracking reveals, for the first time, the dynamic radial migration of the GCs and JGNs, and a unique switch of migration patterns in adult-born JGNs: from radial to long-range lateral migration. Thus, our findings shed new insight on the behavior of adult-born neurons before their integration in the pre-existing neural network.

Results

The use of oCPS for long-term in vivo tracking of individual cells

Specific multicolor labeling of individual adult-born neural stem cells was achieved using red-green-blue (RGB) cell marking approach, utilizing simultaneous, viral vector-mediated expression of genes encoding fluorescent proteins (FP) in the three basic colors mCherry (red), Venus (green) and Cerulean (blue) [21]. To enable monitoring of RGB-marked cells by means of in vivo two-photon imaging, we examined the excitation/emission spectra of each fluorophore. Because of an overlap between the emission spectra of Venus and Cerulean (Figure 1A), excitation splitting was used to differentiate between these two dyes (Figure 1B) such that the sequential scanning of the specimen with 800 and 990 nm excitation light allowed the acquisition of non-overlapping fluorescence signals from each of the three FP (Figure 1C). We first tested this strategy in vitro (HEK-293 cells; Supplementary information, Figure S1A) and then in vivo after retroviral labeling of the adult-born cells in the RMS (Figure 1D and 1E). Under our setting (blue: excitation: 800 nm\emission: dichroic mirror 570 nm, short pass (DM570SP); and green: excitation 990 nm\emission: DM570SP), there was a clear

distinction between fluorescence signals from Cerulean and Venus (Figure 1D). Adding the red channel (800 nm excitation\emission: dichroic mirror 570 nm, long pass), we were able to perform signal collection from the three RGB fluorophores in a time-efficient way (Figure 1E).

Next, we addressed the issue of landmarks in the brain. Blood vessels have been constantly used for this purpose, but traditional angiography involves the intravenous injection of fluorescent dyes [22, 23], which can hardly be performed on a daily basis for long-term cell tracking. Therefore, we used the intraperitoneal route for administration of fluorescent dyes [20, 24]. The examination of a few fluorescent dyes led us to choose sulforhodamine B, which could be effectively excited by two-photon laser and could be cleared from the body in a few hours, allowing enough acquisition time [20] while minimizing potential side effects, if there were any. To make angiography compatible with RGB marking, we chose 900 nm for simultaneous excitation of sulforhodamine B, Venus and Cerulean (Supplementary information, Figure S1B-1D). Since adult-born cells positive only for mCherry constitute only 7.2±9.9% of the whole labeled cell population (see below), the position information for the majority of RGB marked cells could still be obtained. Thus, the sequential scanning of the OB with 800 nm, 990 nm and then 900 nm (after intraperitoneal sulforhodamine B injection) generates sufficient spectral and positional information for long-term single cell tracking, constituting the optical cell positioning system.

oCPS reveals an active migration of adult-born neurons in the olfactory bulb

To evaluate the effectiveness of oCPS for tracking of adult-born cells in the OB, the mixture of the RGB retroviral vectors was injected into the RMS (Figure 2A) where adult-

born cells are actively dividing [18, 20, 25]. Stochastic transduction of cells by the three retroviruses labeled them in one of seven easily distinguishable colors (three basic colors: red, green blue, four mixed colors: yellow, cyan, violet, and white; (Figure 2B-2C)), whereas angiography allowed us to identify the position of each RGB-marked cells (Figure 2B, right). The relative fraction of cells labeled with a given color depends on many factors including viral titer, diffusion properties after injection, cell-cycle status, expression of anti-viral restriction factors, etc. [26, 27]. Data collected from 6 mice (34-136 cells/mouse) indicated that under our experimental conditions around a quarter of FP-positive JGNs were triple-labeled (23.7±3.6 %, here and till the end of this paragraph mean±s.e.m.), 6-19% double labeled (GB 18.9±15.2%; RB 6.5±11.3%; RG 12.2±6.6%) and 7-16% were labeled by a single color (G 9.0±7.5%; B 16.2±15.3%; R 7.2±9.9%; Figure 2C). The sparse nature of the intra-RMS infection of adult-born cells with retroviruses (e.g. Figure 2) further improved the fidelity of cell tracking. In addition to the spectral information (color ID), a few other clues were used for recognition of the same cells in consecutive imaging sessions, such as soma size, morphology of processes, and the existence of stationary cells in the neighborhood. Thus, through sequential collection of spectral and positional information for each RGB-marked cell, each cell received a color hue as well as coordinates in 3D in relation to surrounding landmarks.

Using oCPS, the RGB-labeled cells were imaged every 12 hours starting from 6 days post injection of the virus mixture (DPI 6). We measured a net displacement of the cell's soma in 12 hours (i.e. the migration speed) and found that during the first few days after arrival at their destination layers the migration speed of adult-born cells was high. Adult-born JGNs, for example, migrated 54.8±57.8 μm and 43.7±42.9 μm during 0-0.5 and 0.5-1.0 days in the layer, respectively (Figure 2D, n=65 cells, 5 mice). Under similar recording conditions adult-born granule cells (GCs) traversed 45.6±43.2 μm and

28.4±19.0 µm, respectively (n=141 cells, 5 mice; Figure 2E). It has to be noted, however, that due to the limited depth penetration of our imaging system adult-born GCs were first visualized in the middle of the granule cell layer (~350 µm below the dura). Together, oCPS proved to be a reliable single-cell tracking platform, and has revealed the active migration of adult-born cells in the OB upon arrival at their target layers.

Adult born JGNs switch from radial to lateral migration in the glomerular layer

To characterize migration features of individual cells in more detail, we plotted the migration trajectory of adult-born cells with dots representing the cell's positions during consecutive imaging sessions (Figure 3A, 3B, 3E and Supplementary information, Figure S2). When plotting the mean migration angle (defined in Figure 3C) for each JGN, we found that in the glomerular layer (GL) 97.3% of adult-born JGNs tested (n= 225 cells) migrate at mean angles between 50º and 130º with a clear peak at 80-90º. These data indicate that lateral migration is the preferred migration mode of adult-born cells within the glomerular layer. Below GL, JGNs migrated at much sharper angles (Figure 3A-3C). Paired comparison of mean migration angles of the individual JGNs below and within the GL showed that the mean migration angle within the GL was significantly higher compared to the one below GL (Figure 3D; $P<0.001$, Wilcoxon matched pairs test), suggesting that adult-born JGNs switch from radial to lateral migration after entering the GL.

In contrast, adult-born GCs underwent only radial migration (Figure 3E). The majority (91.7%) of adult-born GCs migrated at the mean angle between 0º and 60º, with a distribution of migration angles centered at 20º-30º (Figure 3F). Comparison of migration angles between JGNs migrating in the GL and GCs migrating in the granule cell layer (GCL) confirmed that the former population migrated at almost right angles (85.0±13.0º,

n=225 cells, 5 mice) and the latter at sharp angles (28.7±24.3º, n=144 cells, 5 mice), with a significant difference between the two (Figure 3G; *P*<0.001, Mann-Whitney test).

Together, these results clearly show that adult-born JGNs undergo a switch in the pattern of their migration: from radial migration below GL to lateral migration within GL, whereas adult-born GCs only migrate radially up to their target locations in the GCL.

Lateral migration patterns of adult-born JGNs in the glomerular layer of the OB.

Next, we examined the lateral migration pattern of adult-born JGNs in more detail. Out of 213 cells dwelling within the fields-of-view (FOVs) between DPI 6 and 60 (data set acquired ≥ every 12 hours), 51.3±5.1% (mean±s.e.m., n=5 mice) displayed saltatory migration pattern, defined as alternating fast moving and stationary periods (Figure 4A, 4B [10]). The remaining cells always changed their position between the imaging sessions. Sixty-two out of 213 cells stayed within the FOVs during the entire recording period, while the others did not (likely moved out of the FOV or died). Of these 62 cells (Figure 3B), 64.2±13.0% showed saltatory migration.

To get a closer insight into the temporal migration pattern of JGNs we imaged them every 15 min over 4 hours on 8, 14, 20 and 30 DPI in another set of experiments (Figure 4C-4J). Out of 49 cells imaged on DPI 8 only 34.5±17.5% of cells (n=5 mice) changed their position during the 4-hour-long recording period, consistent with a notion that cells can remain still for hours and days (Figure 4A, 4B). On DPI 14 these were only 14.0±4.1% and very few cells were moving at later time points (DPI 20-30, see below). Of note, both at DPI 8 and 14 all migrating cells (n=17 and 18, respectively) showed saltatory migration pattern, characterized by alternating stop-and-go phases (Figure 4D-4F). The migration speed of individual cells varied between 4.8 and 28.8 μm/15 min, with median (Figure 4G, *P*≤0.01, Mann-Whitney test), but not maximum (Figure 4H, *P*=0.1, Mann-

Whitney test) migration speed decreasing significantly between DPI 8 and DPI 14. At the same time, there was no significant difference in the maximum duration of individual stationary periods (Figure 4I) as well as the cumulative duration of a stationary phase within the 4-hour observation window (Figure 4J) between the two age groups (P=0.83 and 0.24, respectively, Mann-Whitney test). Note, however, that cells of both age groups spent more than 80% of their time at rest (DPI 8: 81±22%, n=17 cells, 5 mice; DPI 14: 88±11%, n=18 cells, 5 mice). In the remaining time the cells were migrating at a median speed of 9.9±4.8 μm/15 min (DPI 8) and 6.7±5.2 μm/15min (DPI 14, Figure 4G). Taking into account long resting intervals of migrating JGNs and the fact that 100% of cells migrating during the 4-hour-long recording period showed saltatory migration pattern, we concluded that saltatory migration is the main temporal migration pattern of adult-born JGNs within the GL.

The spatial migration patterns of individual adult-born JGNs were highly variable (Figure 5A and Supplementary information, Figure S2, S3A-S3C). For quantification, we used two different procedures first quantifying the maximal angle (θ) between the two immediate migration steps and second, quantifying the ratio between the net (the distance between the cell's entry point in the GL and its final location) and total distances traversed by the cell. For the first method, if θ was ≤ 90º, the migration of the cell was categorized as unidirectional (Figure 5B, upper panel); otherwise, as multidirectional migration (Figure 5B, lower panel). The unidirectional group included cells showing little change in the direction of their movement, whereas the multidirectional cells underwent abrupt changes in the direction of the migration. On average, 43.7±1.5 % (here and till the end of this paragraph mean±s.e.m., n=93/213 cells in 5 mice) of migrating cells were unidirectional and the remaining 56.3±1.5% were multidirectional (Figure 5C). Of these, saltatorily migrating cells constituted 60.8±4.8% and 41.6±4.4% of multi- and uni-directionally migrating groups, respectively, pointing towards preferred saltatory behavior

of multi-directionally migrating cells (Student's t test, $P<0.05$, n=5). Among the cells that remained within the FOVs for the entire recording period (62 cells, 5 mice), 55.5±5.8% and 44.5±5.8% were multi- and uni-directionally migrating cells, respectively. These numbers are similar to the ones obtained for general population (paired t test, $P=0.9$ for either migratory behavior).

In the second categorizing method (established by Nam et al. [15]), cells were subdivided into "migratory", "exploratory" and "intermediate" according to the ratio of the net to the total distance traversed (migratory: 0.6-1.0; exploratory: 0.0-0.4; intermediate: 0.4-0.6). Out of 213 recorded cells (n=5 mice) 62.7±3.2% were "migratory", 16.5±3.5% "intermediate", and 20.5±2.4% "exploratory" cells (mean±s.e.m., Supplementary information, Figure S3D). We found that there was no significant difference in the net migration distance between unidirectional (Figure 5D, 120.0±106.5 μm, n=93 cells, 5 mice) and multidirectional cells (114.0±149.5 μm, n=120 cells, 5 mice, $P=1.0$, Mann-Whitney test). However, the cumulative distance (summation of all migration steps in the GL) in multidirectional group (225.0±263.5 μm, n=120 cells, 5 mice) was significantly larger than that in unidirectional group (Figure 5E, 133.0±112.0 μm, n=93 cells, 5 mice, $P<0.001$, Mann-Whitney test).

When comparing the two categorizing methods, we found that virtually all cells (97.2±2.0%) in unidirectional migration group were "migratory", with a small fraction (2.8±2.0 %) going to the "intermediate" group (Supplementary information, Figure S3E). None of them were "exploratory" cells. In contrast, cells in multidirectional migration group were scattered among "migratory", "intermediate" and "exploratory" groups (35.2±4.7%, 27.7±4.9%, and 37.1±4.4%, respectively; n=5 mice).

Taken together, these results show that adult-born JGNs undergo stereotyped migration patterns during their lateral movement in the GL: saltatory migration on a temporal scale, and uni- or multidirectional migration on a spatial scale. Although the

total distances traversed reached up to 900 μm, the cells usually settled down about 1-2 glomeruli apart from the point where they initially entered the GL.

Odor-deprivation does not affect the migration of adult-born JGNs.

Having characterized the lateral migration pattern of adult-born JGNs in the GL, we next asked if any of the migration parameters (speed, pattern or distance) are sensitive to global changes in the sensory input. To answer this question, we used unilateral naris closure on DPI 6 and compared the migration properties of adult-born JGNs from either the odor-deprived (OD) side or non-OD OBs as control. The OD group included only those bulbs (n=4), in which naris occlusion resulted in a significant decrease in the expression of tyrosine hydroxylase (TH), confirmed immunohistochemically (Supplementary information, Figure S4A, S4B). Despite a clear reduction in TH expression in OD bulbs, a known consequence of the naris closure [28, 29], there was no significant difference in migration speed between the cells in control and OD groups (Supplementary information, Figure S4C). Similarly, we did not observe any difference in mean migration angles (Supplementary information, Figure S4D), the fraction of cells with uni- or multidirectional migration patterns (Supplementary information, Figure S4E), and net or cumulative distances that cells traveled in the GL (Supplementary information, Figure S4F). Taken together, these data suggest that the pattern of lateral migration of adult-born JGNs is not sensitive to an overall decrease in the strength of sensory input.

Layer-specific migratory behavior of adult-born neurons

We next focused on the migration of adult-born neurons below GL: in the EPL and in the GCL (Figure 6). We analyzed cells that were first identified when migrating inside the

GCL and then monitored until they took up their final position in either the GCL or the GL (e.g. Supplementary information, Figure S2). First, we compared the mean migration speed of future JGNs in three different layers of the OB: within GCL, through EPL, and within GL. Neuroblasts migrating towards GL moved significantly faster in the EPL when compared to their migration in the two other layers (median migration speed through EPL: 118.0±82.0 µm, within GCL: 66.0±53.0 µm, and within GL 41.0±30.0 µm; Figure 6A). As for the migration angle, there was no significant difference between GCL and EPL, in which cells migrated rather vertically (within GCL: 27.0±24.0º, through EPL: 34.9±27º, P=0.1, Kruskal-Wallis test followed by Dunn's multiple comparison test; Figure 6B). However, the migration angle in the GL (84.0±18.0º) was significantly different from the former two (P<0.001, Kruskal-Wallis test followed by Dunn's multiple comparison test, n=43 cells with paired data, 4 mice), consistent with the lateral migration of adult-born cells in the GL (see also Figure 3C for non-paired data sample).

Next we asked whether the cells going to become either adult-born GCs or JGNs display different migratory behavior when migrating in GCL. To answer this question, we compared the speed and migration angles of the two cell types. For adult-born GCs the day they settled down at their final position was defined as day 0, while for adult-born JGNs, day 0 was the day they exited GCL. It turned out that 1.5-0.5 days before settlement or exiting GCL both cells population had very similar migrating speed (Figure 6C-6D). However, on days 0.5-0 GCs slowed down, while JGNs speeded up to exit the GCL. This opposing trend resulted in a significant difference in the migration speed between the two cell populations (Figure 6D, P<0.001, Mann-Whitney test). As for mean migration angle, no difference was found between JGNs and GCs when they were migrating in GCL (Figure 6E).

These results suggest that future granule and juxtaglomerular cells show similar migration properties when in GCL. The differences are seen only during the last half a day, when the decision to settle down and to become a GC or to speed up and to leave the GCL becomes obvious.

Gradual settlement of adult-born neurons in the olfactory bulb

Next, we examined the general motility of the population of adult-born neurons over time. Soon after arrival of the cells at their destination layer (Figure 7A-7B; upper panels) the majority of adult-born cells were mobile, changing their position between the imaging sessions. Plotting the fraction of moving cells over time clearly showed a gradual decrease in the motility of both adult-born JGNs and GCs (Figure 7A-7B; lower panels). Since the fraction of mobile cells was below 5% from DPI 30 onwards, we defined cell populations at DPI 30+ as stable populations and plotted the fraction of stable population as a function of time (Figure 7C). We observed a gradual accumulation of stable population both for JGNs and GCs. However, the adult-born GCs seemed to settle down significantly earlier than JGNs (Kolmogorov–Smirnov test, $P \leq 0.05$). The time required to achieve 90% of stable population was significantly shorter for GCs compared to JGNs (Figure 7D, DPI 18.0±5.75 days for GCs, vs DPI 26.0±4.0 days for JGNs, Mann-Whitney test, $P<0.01$).

At the level of individual adult-born cells we compared the length of the first migration step within the destination layer with the length of the last migration step before settlement and found significant difference between the two both for JGNs and GCs (Figure 7E). No significant difference was found between the length of either first or last step when comparing JGNs and GCs to each other (Mann-Whitney test, $P=0.92$ and 0.76, respectively).

Taken together, our data show that adult-born neurons gradually decrease their migration speed as they mature and settle down to form a stable population. In mice this process lasts approximately 4 weeks for JGNs and approximately 3 weeks for GCs.

Discussion

A huge challenge for long-term in vivo cell tracking is to identify the same cells at different time points (identity), and to precisely target the cell's position (location). The optical cell positioning system introduced here addresses both issues enabling monitoring the behavior of individual cells in their native environment over prolonged (weeks to months long) periods of time. For quantifying the fidelity of the RGB marking when using seven easily distinguishable colors, we used JGNs as an example. First, we measured the distribution of the distances between the two consecutive positions of each juxtaglomerular cell (step distance) for all imaging sessions (Supplementary information, Figure S5). The median distance was 41.95 ± 49.95 (IQR) µm, with only 10% of step distances being larger than 109 µm. Next, we determined the fraction of cells having the same color code (out of 7 colors mentioned above) and located at the same DPI in the same field of view at the distance smaller that 109 µm. Out of the total 225 cells analyzed in this study, we found 16 cases (16 pair of cells, i.e. 32 cells), amounting to 14.2 % of the total population. We concluded therefore that for the vast majority of cases (85.8 %) the RGB marking with 7 distinct colors allows precise tracking of individual cells. In fact, the slowing down of the cells in the course of migration (Figures 4A and 7E) and existence of a number of additional criteria (e.g. the soma size, the direction of the leading process as indicator of migration direction, the ratio of the fluorescence recorded in different channels (proportional to the number of incorporated virus copies and the strength of FP expression) and the existence of stationary cells in the neighborhood) reduce the ambiguity in the system even further. It has to be noticed

that the RGB marking approach is not genuinely restricted to 7 colors and, as was shown previously [21, 26], can provide a huge number of different color hues. The precise readout of these hues, however, requires more sophisticated imaging and color-identification approaches, which seem unnecessary within the framework of the present study. Importantly, the oCPS is not restricted to RGB marking, it is possible to adapt this strategy to other labeling methods for identification of individual cells, such as Brainbow [30] and MAGIC [31]. Furthermore, the oCPS is also not restrained to the OB and has the full potential to be applied to other regions of the brain, or the body, making it a promising approach for long-term tracking of cells of other lineages.

Our novel experimental approach enabled us to identify migrating cells deep within the OB and to follow their migration until arrival at their final destination within the GCL or the GL. Our data (graphically summarized in Figure 8) suggest that immediately after exiting RMS, all adult-born neurons are very similar in their migratory behavior. They migrate radially towards the surface of the bulb with future GCs and JGNs migrating at a similar speed. The difference in the migratory behavior of the two cell types first becomes evident when adult-born JGNs are about to leave the GCL: JGNs considerably speed up, whereas the adult-born granule cells slow down and eventually settle within the GCL. The JGNs traverse the EPL at the highest speed observed during the entire migration period monitored in this study, slow down when entering GL and switch to lateral migration. Although phenomenologically the lateral migration of the adult-born JGNs within the GL is similar to tangential migration of immature GABAergic interneurons during embryonic development [10], we use the word *lateral* to avoid misunderstanding, because the word *tangential* is widely used for migration of neuronal precursor cells in the RMS [4].

Our direct observation of in vivo dynamics of adult stem cells behavior uncovered the switch from radial to lateral migration for adult-born JGNs and the long-range lateral

migration itself, that could not be inferred from the literature. In contrary, the literature data postulate that adult-born cells (JGNs as well as GCs) either undergo radial migration only [3, 4, 9] or first migrate predominantly to the glomerular layer before populating the granule cell layer [18]. In contrast to what could be inferred from the *in vitro* data [15], our results uncover a surprisingly vigorous migration of the adult-born JGNs in the GL. Around 40% of adult-born JGNs undergo unidirectional migration without abrupt changes in migration direction ending up somewhere one-to-two glomeruli away from the initial entry points. Unidirectional migration is similar to the directed migratory behavior of neuroblasts in the RMS of juvenile/adult mice [15], albeit happening at a slower speed (see below). It is therefore not surprising that 97.3±2.0 % of unidirectional cells showed migratory behavior, when analyzed according to criteria used by Nam et al. [15]. The remaining 60% of adult-born JGNs underwent multidirectional migration, traveling up to 900 µm in terms of cumulative distance, before they also settled down one-to-two glomeruli away from the initial entry points (Figure 8). The multidirectional migration mode is reminiscent of the “multipolar” migration mode described for the embryonic cerebral cortex [32]. In both cases the cells migrate in various directions and change their direction frequently, but generally move away from their original location. This differs from the exploratory behavior of neuroblasts in the neonatal, juvenile and adult SVZ [11, 15], where the frequent direction change results in large cumulative but rather small net displacement of the cell body. Consistently, only 20.5% of JGNs were exploratory under our experimental conditions. The multidirectional migration mode seems to be a hallmark of adult-born JGNs, as we have never observed multidirectional migration in adult-born GCs. The latter migrated radially without direction change (unidirectional migration) and gradually settled down in the GCL.

In the temporal dimension, both adult-born JGNs and GCs exhibited saltatory stop-and-go movement, typical for many types of migrating cells [10, 33]. In previous *in vitro*

studies the intermittent stops during the migration of individual cells were rather brief, giving an impression of a continuous movement [11, 15, 34, 35], but many JGNs analyzed here stopped for very long time periods (from 12 hours to a few days) before resuming the further movement. Continuous imaging of the cells at high temporal resolution, i.e. every 15 minutes, revealed that cells were migrating at a median speed of 0.4-0.8 μm/min. Scaling up to μm/h one would obtain the median migration speed of 24-48 μm/h, which is comparable to values obtained in organotypic slices from perinatal mice for cells detaching from the RMS and starting radial migration into the bulb [12], or for SVZ neuroblasts migrating in exploratory/intermediate fashion in acute OB slices from juvenile/adult mice [15]. At the same time, these values are lower than the ones obtained in different studies of RMS migration (from 40-60 to 70-150 μm/h [12, 15, 16, 36]). In between the migration steps, the cells remained stationary for prolonged periods of time (with individual stationary periods lasting more than 80% of the total observation time). This finding together with the skewed migration trajectory of the cells explains why within 12 hours cells translocated much less than can be expected from a simple scaling up of their migration speed. Interestingly, the median migration speed decreased significantly as the time passed by, paralleled by a decrease in the size of migration step per 12 hours and in the fraction of migrating cells. Taken together these data suggest that general motility of adult-born JGNs is age dependent and decreases as the cells mature.

Our population analysis has pinpointed a time window during which adult born cells are actively migrating, possibly seeking integration targets. This period of time, which we named “pre-integration phase”, is characterized by a vigorous migratory behavior of adult-born cells, long-distance lateral migration of JGNs with characteristic temporal (stop-and-go) and spatial (migratory, uni- or multidirectional) patterns and odor responsiveness [20] of migrating cells. Lasting for 3-to-4 weeks, pre-integration phase is

the time period of initial fate determination of adult-born cells, critically impacting on the location of cell's settlement, their odor-responsiveness (for JGNs predetermined by the glomeruli in which they integrate [37]) and likely also their survival rate. Several lines of evidence suggest that the pre-integration phase plays an important role in defining the functional properties and the fate of adult-born neurons. During the early pre-integration phase the migratory behavior of adult-born cells is stereotypic and is likely to be driven by the molecular clues [18, 38]. Only a few days later, however, migrating JGNs (and likely also GCs) become responsive to sensory stimuli [20]. From now on the migration of adult-born JGNs is likely to be driven both by extrinsic sensory stimuli and by intrinsic molecular clues, some of which, however, also depend on sensory stimuli [18, 39]. On the other hand, global migration parameters of JGNs (e.g. migration angle and speed, net and cumulative distance traversed) were similar in the presence and the absence of the extrinsic sensory input. Since the radial migration of adult-born granule cells was not affected by odor-deprivation either [17], it is likely that the overall strength of olfactory input does not affect the long-range migration within the OB. However, considering preferential incorporation of adult-born neurons into active neural circuits in the dentate gyrus [40] and activity-dependent expression of tenascin-R, a molecular marker controlling migration of neuroblasts in the OB [18], we postulate that local activity patterns, rather than overall strength of the signal, might influence migration properties of adult-born cells. Together the extrinsic stimuli and intrinsic factors might govern the adult-born JGNs to active glomeruli and orchestrate their survival/integration therein.

Taken together, our data has overthrown the classical migration model of adult-born cells in the olfactory bulb, revealing vivid radial migration of GCs and a unique radial-to-lateral switch in migration patterns of adult-born JGNs. In addition, it introduced the pre-integration phase which overlaps with the critical period for maturation of adult-born cells (around 10-25 days after birth), when sensory activity critically impacts on their survival

[39, 41, 42]. Our study has opened new fields of investigation for (i) understanding the mechanisms underlying lateral migration and its implication for adult neurogenesis (ii) using this new knowledge for developing/testing new strategies in stem cell therapy.

Materials and Methods

Ethics Statement

All experimental procedures involving the handling and use of mice were performed in accordance with institutional animal welfare guidelines and were approved by the state government of Baden-Württemberg, Germany.

Animals and cranial window for optical imaging

Male 3-6 months old C57/BL6 mice were implanted with a chronic cranial window as described earlier [20]. Briefly, mice were anesthetized by intraperitoneal (i.p.) injections of ketamine/xylazine (80/4 µg/g body weight (BW); Fagron, Barsbuettel, Germany, and Sigma, Sigma-Aldrich, St Louis, MO, respectively). Anesthetic depth was monitored by toe pinch throughout the surgery and additional ketamine/xylazine (40/2 µg/g of BW) was injected when necessary. Dexamethasone (2 µg/g BW, Sigma-Aldrich) was administered i.p. before the surgery and lidocaine (2%, AstraZeneca, Wedel, Germany) was applied subcutaneously before removing the scalp over the OB. A circular groove (3 mm in diameter) was made with a microdrill over the two OB hemispheres by repeated drilling. Then the skull over each side of the OB was gently removed with tweezers. Extreme care was taken not to damage the blood vessels at the caudal part of the OB. Standard extracellular solution (125 mM NaCl, 4.5 mM KCl, 26 mM $NaHCO_3$, 1.25 mM NaH_2PO_4, 2 mM $CaCl_2$, 1 mM $MgCl_2$ and 20 mM glucose, pH 7.4 when bubbled continuously with 95% O_2 and 5% CO_2) was used to rinse the opening in the skull, which

was then covered with a 3 mm glass coverslip (Warner Instruments, Hamden, CT). The gap between the edge of the coverslip and the skull was filled with cyanoacrylate glue, and then strengthened by dental cement. During the surgery, and until full recovery, the mouse was kept on a heated plate with temperature of 38º C. Postoperative care included an analgesic dose of carprofen (5 µg/g BW, Pfizer, Berlin, Germany) for three days subcutaneously and the antibiotic baytril (Bayer, Leverkusen, Germany; 1:100 v/v) in drinking water for ten days. Mice were allowed to recover for at least three weeks and were subsequently examined for window clarity and new bone growth. Those mice that passed the quality control were injected with retrovirus into the RMS.

Retroviral vector production

Design, production and application of retroviral vectors are described in detail in ref. [27]. Briefly, the viral vectors were derived from the γ-retroviral vector RSF91.GFP.pre* [43], whose marker gene (eGFP) has been replaced by one of the three fluorescent proteins Cerulean, Venus and mCherry, driven by an enhancer/promoter from the spleen focus-forming virus within the long terminal repeats. Vector maps and sequence data for all vectors are available upon request; more information can be found at http://www.LentiGO-Vectors.de. Cell-free supernatants containing viral particles were produced by transient transfection of HEK-293T packaging cells as described previously [26, 43]. Retroviral vectors have been packaged using pcDNA3.MLVgp and phCMV-VSV-G. In some sets of experiments, retrovector encoding eGFP driven by CAG [44] was utilized and packaged by 1F8 cells derived from 293GPG cell line [45]. Supernatants containing retroviral particles were concentrated about 100-fold by centrifugation at 8,000×g and 6°C for 8 to 12 hours. Concentrated supernatants were titrated [26] on 293T cells. For titration, 293T cells were incubated at 5×10^4 cells in 0.5

ml medium in each well of a 24 well plate in the presence of 8 µg/ml polybrene. After addition of particle-containing supernatant, the plate was centrifuged at 1,000×g for 1 hour at 25°C. Initial gene transfer rates were analyzed 48 to 72 hours after transduction by FACS. To acquire FACS data, the cytometer LSRFortessa (405/488/561/640 nm lasers) was used (Becton Dickinson, Heidelberg, Germany). Titers of about 8×10^9 virus particles per ml concentrated supernatant were obtained for the vectors used (range: $6.6\text{-}9.8 \times 10^9$ v.p./ml).

Retroviral vector injection into the RMS

Animals with a chronic cranial window over the OB were anesthetized as above and fixed to a stereotaxic device (Stoelting, Wood Dale, IL) by ear bars, and 2% lidocaine was applied subcutaneously to the skin overlying the left and the right injection sites. The dental cement covering the injection sites was removed by drilling. Premixed retrovectors (1.5 µl, 1:1:1 for retrovectors encoding the three fluorescent proteins with different colors) or the retrovector encoding eGFP were stereotactically injected into the RMS at the following coordinates: anteroposterior: +3.0 mm from Bregma, mediolateral: ±0.82 mm, and -2.9 mm from pial surface [20]. Then a metal bar for head fixation was fixed to the caudal part of the skull with dental acrylic and cement. The other exposed parts of the skull were also covered with dental cement. The mice were returned to the home cage, and carprofen (5 µg/g BW, Pfizer) was injected subcutaneously for three days.

Odor-deprivation and two-photon imaging of odor-deprived mice

In mice with RGB-marked adult-born neurons, unilateral naris closure was performed on DPI 6 using well established technique [29]. The nasal septum separates the left and the right nasal cavities and olfactory sensory neurons project exclusively to the ipsilateral OB. Therefore, unilateral naris closure blocks the sensory inputs to the ipsilateral OB [29]. Animals were anesthetized by ketamine/xylazine as described above. Nose plugs were constructed out of small bits of polyethylene tubing (1.5 mm in diameter) which were closed at one end by heating before insertion, and inserted into the right or left external naris of mice. After insertion of the plug, the animals were returned to their home cages. From DPI 6 (first day of occlusion) to DPI 16, the OBs from either side of the brain were imaged according to procedures described below to track the migration of the RGB-marked adult-born neurons. Three to five fields of view were acquired from each side of the OB and in each FOV, 5-20 cells were tracked. At endpoints, mice were transcardially perfused with 4 % paraformaldehyde and brains were cryoprotected in 25 % sucrose overnight. Coronal slices (40 μm) were obtained by cryosectioning the OB. The expression level of tyrosine hydroxylase (TH) in either side of the OB was examined through immunostaining with antibody against TH (Millipore, Billerica, MA).

In vivo imaging and OBPs setup

Mice with chronic cranial windows were anesthetized with isofluorane (2.5 % for induction, 0.8-1.5 % for maintenance). Breathing rate and body temperature were monitored continuously using the anesthesia monitoring system from AD Instruments (Sydney, Australia). The head of the mouse was fixed through the metal bar to the X-Y table, ensuring consistent positioning through imaging sessions. *In vivo* two-photon

imaging was performed using a customized microscope based on Olympus FV1000 system (Olympus, Tokyo, Japan) and MaiTai Deep See Laser (Spectra Physics, Mountain View, CA), with a Zeiss x 20 water-immersion objective lens (NA 1.00). The adult-born cells were imaged starting from DPI 6 according to the following protocol: every 12 hours (DPI 6-DPI 15), every 24 hours (DPI 15-DPI 20), every 2 days (DPI 20-DPI 30) and once a week (DPI 30-DPI 60). Each imaging session lasted ~2 hours. The oCPS approach combined two complementary techniques: multicolor single cell imaging and blood vessel visualization. We used following setting to split fluorescence emitted by FP-labeled adult-born cells: Red: excitation: 800 nm / emission: long-pass (LP) channel of 570 nm dichroic mirror (DM570); Green: excitation: 990 nm / emission: short-pass (SP) channel of DM570; Blue: excitation: 800 nm / emission: SP channel of DM570. To create landmarks for single-cell tracking, we visualized blood vessels in the OB through intraperitoneal injection of sulforhodamine B (0.1 ml / 10 g body weight, 1 mM in PBS, Sigma-Aldrich). One single injection enabled visualization of blood vessels for around 2 hours. The acquisition setting for sulforhodamine B was: excitation: 900nm / emission: LP channel of DM570. In practice, each FOV (636 µm x 636 µm, from dura to 350 µm) was sequentially scanned with 800 nm and 990 nm. Then, sulforhodamine B was injected and the same FOV was scanned again with 900 nm. As shown previously (Suppl. Fig. 2 in ref. [20]) blood vessel pattern is very stable over prolonged periods of time, providing a reliable framework for long-term tracking of individual cells.

Data analysis

The combined three-dimensional blood vessels/cells image stacks (e.g. Supplementary information, Figure S3A-C) acquired during the consecutive imaging sessions were aligned offline using the blood vessel pattern as an anatomic landmark (see

Supplementary Figure 2 in ref. [20]). Due to the stability of this landmark throughout the imaging series, the alignment errors (estimated by comparing images of stable cells at DPI 28 and 30) did not exceed 1.25 – 2.5 μm in X-Y direction and 2-4 μm in Z direction. Cells located up to a depth of 120 μm under the dura were regarded as adult-born JGNs, while the cells below mitral cell layer were taken as adult-born GCs (unless they were retrospectively found to be migrating JGNs). Each cell was annotated with an identity number. The color hue of each cell was determined as described above. Cells from the consecutive time points were tracked according to their RGB spectrum, location, and size throughout the 33 time points from DPI 6 to DPI 60, generating a series of annotated stacks. Then, according to annotated stacks, the history and trace of each single cell was sorted out. The center of cell's soma in each annotated stack was marked as a position point, and then the cell's trajectory was reconstructed based on its position points in all annotated stacks of the same FOV. Next, the X-Y coordinates for each position point of a cell were read from Fluoview 3.0 Viewer (Olympus). For Z axis coordinates, the depth of cells (Z_{ac}, actual depth of a cell) was the relative depth from the dura: $Z_{ac} = Z_{reading} - Z_{dura}$. With 3D coordinates for each track point, migration distance (D) between two points in space was calculated by the following formula:

$$D = \sqrt{(X1 - X0)^2 + (Y1 - Y0)^2 + (Z1 - Z0)^2}$$

where (X1, Y1, Z1) and (X0, Y0, Z0) were coordinates of the target cell position measured at current or previous temporally-consecutive stacks, respectively. Unless otherwise indicated, migration speed was defined as the translocation of cell's soma between the two consecutive sessions divided by the respective time period. Taking into account the 2 μm step size of the acquired stacks, a cell was considered moving if the translocation of cell's soma between the two consecutive sessions was more than 4 μm.

The migration angle (α) between migration direction and Z axis was calculated by the following formula: $\alpha = \arccos((Z_1-Z_0)/D)$. In our experiments Z axis (the optical axis of the objective) deviated slightly (by γ = 4.36±4.11° median, IQR (see Supplementary methods for the description of γ estimation procedure)) from the radial axis of the bulb (n=206 image stacks). This deviation, however, was too small to affect the quality of data analysis (not shown).

To categorize the migration modes of JGNs in GL, two methods were used. One method [15] binned cells into migratory, exploratory and intermediated cells according to the ratio of the net distance a cell has traversed to the total distance it has traversed: migratory behavior 0.6-1.0, exploratory 0.0-0.4, and the intermediate 0.4-0.6. The other one, which we proposed, defined two types of migration modes based on the maximal migration angle (θ) between the two immediately adjacent migration steps. If θ was ≤90º, then the migration of the cell was categorized as unidirectional, otherwise, as multidirectional. For plots of the fraction of moving cells at a certain time point, the proportion of cells, whose positions differed from that recorded at immediately preceding time point, was calculated in relation to the total number of cells in that stack. 3D cell trajectory and 2D plot of cell migration speed were generated by IGOR Pro (WaveMetrics, Portland, OR). Projected images from stacks were processed by ImageJ software (http://rsb.info.nih.gov/ij/).

Statistics

Statistical analysis consisted of the following: Shapiro-Wilk (n≥7) or Kolmogorov–Smirnov (n≥ 5) normality tests. For normally distributed data, mean ± s.e.m. was calculated and student's t test was used for comparison of two groups. For data that were not normally distributed, median ± one interquartile range was presented as box

plot, and 10 to 90 percentiles were shown as whiskers. In the text all data are presented as median ± interquartile range, unless otherwise indicated. Nonparametric tests were used for comparisons between not normally distributed data sets. Mann-Whitney test was used for comparison between the two groups and Kruskal-Wallis nonparametric test was used for comparison between more than two groups followed by the Dunn's multiple comparison test. Wilcoxon matched pairs test was used for nonparametric comparison of two paired samples. All the statistical tests were two sided. Significance level was set to $P \leq 0.05$.

Acknowledgments

We thank E. Zirdum, A. Weible, G. Heck and K. Schoentag for technical assistance; F. Gage for the retroviral vector backbone; J. Nabekura for his advice on naris closure protocols, V. H. Perry and J. Sheng for valuable comments on the manuscript. This work was funded by fortüne-Programm of Tübingen University, Nr. 2175-0-0. KR and BF have been supported by SFB841.

Competing financial interests: The authors declare no competing financial interests.

Supplementary information is available at the Cell Research website.

References

1 Lois C, Alvarez-Buylla A. Long-distance neuronal migration in the adult mammalian brain. *Science* 1994; **264**:1145-1148.

2 Lois C, Garcia-Verdugo JM, Alvarez-Buylla A. Chain migration of neuronal precursors. *Science* 1996; **271**:978-981.

3 Alvarez-Buylla A, Garcia-Verdugo JM. Neurogenesis in adult subventricular zone. *J Neurosci* 2002; **22**:629-634.

4 Lledo PM, Alonso M, Grubb MS. Adult neurogenesis and functional plasticity in neuronal circuits. *Nat Rev Neurosci* 2006; **7**:179-193.

5 Lepousez G, Nissant A, Lledo PM. Adult Neurogenesis and the Future of the Rejuvenating Brain Circuits. *Neuron* 2015; **86**:387-401.

6 Whitman MC, Greer CA. Adult neurogenesis and the olfactory system. *Prog Neurobiol* 2009; **89**:162-175.

7 Doetsch F, Caille I, Lim DA, Garcia-Verdugo JM, Alvarez-Buylla A. Subventricular zone astrocytes are neural stem cells in the adult mammalian brain. *Cell* 1999; **97**:703-716.

8 Garcia AD, Doan NB, Imura T, Bush TG, Sofroniew MV. GFAP-expressing progenitors are the principal source of constitutive neurogenesis in adult mouse forebrain. *Nat Neurosci* 2004; **7**:1233-1241.

9 Ming GL, Song H. Adult neurogenesis in the mammalian brain: significant answers and significant questions. *Neuron* 2011; **70**:687-702.

10 Ghashghaei HT, Lai C, Anton ES. Neuronal migration in the adult brain: are we there yet? *Nat Rev Neurosci* 2007; **8**:141-151.

11 Kakita A, Goldman JE. Patterns and dynamics of SVZ cell migration in the postnatal forebrain: monitoring living progenitors in slice preparations. *Neuron* 1999; **23**:461-472.

12 De Marchis S, Fasolo A, Shipley M, Puche A. Unique neuronal tracers show migration and differentiation of SVZ progenitors in organotypic slices. *J Neurobiol* 2001; **49**:326-338.

13 Suzuki SO, Goldman JE. Multiple cell populations in the early postnatal subventricular zone take distinct migratory pathways: a dynamic study of glial and neuronal progenitor migration. *J Neurosci* 2003; **23**:4240-4250.

14 Zhang RL, Chopp M, Gregg SR *et al.* Patterns and dynamics of subventricular zone neuroblast migration in the ischemic striatum of the adult mouse. *J Cereb Blood Flow Metab* 2009; **29**:1240-1250.

15 Nam SC, Kim Y, Dryanovski D *et al.* Dynamic features of postnatal subventricular zone cell motility: a two-photon time-lapse study. *J Comp Neurol* 2007; **505**:190-208.

16 Wichterle H, Garcia-Verdugo JM, Alvarez-Buylla A. Direct evidence for homotypic, glia-independent neuronal migration. *Neuron* 1997; **18**:779-791.

17 Petreanu L, Alvarez-Buylla A. Maturation and death of adult-born olfactory bulb granule neurons: role of olfaction. *J Neurosci* 2002; **22**:6106-6113.

18 Saghatelyan A, de Chevigny A, Schachner M, Lledo PM. Tenascin-R mediates activity-dependent recruitment of neuroblasts in the adult mouse forebrain. *Nat Neurosci* 2004; **7**:347-356.

19 Mizrahi A. Dendritic development and plasticity of adult-born neurons in the mouse olfactory bulb. *Nat Neurosci* 2007; **10**:444-452.

20 Kovalchuk Y, Homma R, Liang Y *et al.* In vivo odourant response properties of migrating adult-born neurons in the mouse olfactory bulb. *Nat Commun* 2015; **6**:6349.

21 Weber K, Thomaschewski M, Warlich M *et al.* RGB marking facilitates multicolor clonal cell tracking. *Nat Med* 2011; **17**:504-509.

22 Christie RH, Bacskai BJ, Zipfel WR *et al.* Growth arrest of individual senile plaques in a model of Alzheimer's disease observed by in vivo multiphoton microscopy. *J Neurosci* 2001; **21**:858-864.

23 Bolmont T, Haiss F, Eicke D *et al.* Dynamics of the microglial/amyloid interaction indicate a role in plaque maintenance. *J Neurosci* 2008; **28**:4283-4292.

24 Masamoto K, Tomita Y, Toriumi H *et al.* Repeated longitudinal in vivo imaging of neuro-glio-vascular unit at the peripheral boundary of ischemia in mouse cerebral cortex. *Neuroscience* 2012; **212**:190-200.

25 Doetsch F, Garcia-Verdugo JM, Alvarez-Buylla A. Cellular composition and three-dimensional organization of the subventricular germinal zone in the adult mammalian brain. *J Neurosci* 1997; **17**:5046-5061.

26 Weber K, Thomaschewski M, Benten D, Fehse B. RGB marking with lentiviral vectors for multicolor clonal cell tracking. *Nat Protoc* 2012; **7**:839-849.

27 Gomez-Nicola D, Riecken K, Fehse B, Perry VH. In-vivo RGB marking and multicolour single-cell tracking in the adult brain. *Sci Rep* 2014; **4**:7520.

28 Baker H, Morel K, Stone DM, Maruniak JA. Adult naris closure profoundly reduces tyrosine hydroxylase expression in mouse olfactory bulb. *Brain Res* 1993; **614**:109-116.

29 Cummings DM, Brunjes PC. The effects of variable periods of functional deprivation on olfactory bulb development in rats. *Exp Neurol* 1997; **148**:360-366.

30 Livet J, Weissman TA, Kang H *et al.* Transgenic strategies for combinatorial expression of fluorescent proteins in the nervous system. *Nature* 2007; **450**:56-62.

31 Loulier K, Barry R, Mahou P *et al.* Multiplex cell and lineage tracking with combinatorial labels. *Neuron* 2014; **81**:505-520.

32 Tabata H, Nakajima K. Multipolar migration: the third mode of radial neuronal migration in the developing cerebral cortex. *J Neurosci* 2003; **23**:9996-10001.

33 Edmondson JC, Hatten ME. Glial-guided granule neuron migration in vitro: a high-resolution time-lapse video microscopic study. *J Neurosci* 1987; **7**:1928-1934.

34 Komuro H, Yacubova E, Rakic P. Mode and tempo of tangential cell migration in the cerebellar external granular layer. *J Neurosci* 2001; **21**:527-540.

35 Schaar BT, McConnell SK. Cytoskeletal coordination during neuronal migration. *Proc Natl Acad Sci U S A* 2005; **102**:13652-13657.

36 Davenne M, Custody C, Charneau P, Lledo PM. In vivo imaging of migrating neurons in the mammalian forebrain. *Chem Senses* 2005; **30 Suppl 1**:i115-116.

37 Homma R, Kovalchuk Y, Konnerth A, Cohen LB, Garaschuk O. In vivo functional properties of juxtaglomerular neurons in the mouse olfactory bulb. *Front Neural Circuits* 2013; **7**:23.

38 Hack I, Bancila M, Loulier K, Carroll P, Cremer H. Reelin is a detachment signal in tangential chain-migration during postnatal neurogenesis. *Nat Neurosci* 2002; **5**:939-945.

39 Khodosevich K, Lazarini F, von Engelhardt J, Kaneko H, Lledo PM, Monyer H. Connective tissue growth factor regulates interneuron survival and information processing in the olfactory bulb. *Neuron* 2013; **79**:1136-1151.

40 Kee N, Teixeira CM, Wang AH, Frankland PW. Preferential incorporation of adult-generated granule cells into spatial memory networks in the dentate gyrus. *Nat Neurosci* 2007; **10**:355-362.

41 Mouret A, Gheusi G, Gabellec MM, de Chaumont F, Olivo-Marin JC, Lledo PM. Learning and survival of newly generated neurons: when time matters. *J Neurosci* 2008; **28**:11511-11516.

42 Yamaguchi M, Mori K. Critical period for sensory experience-dependent survival of newly generated granule cells in the adult mouse olfactory bulb. *Proc Natl Acad Sci U S A* 2005; **102**:9697-9702.

43 Schambach A, Mueller D, Galla M *et al.* Overcoming promoter competition in packaging cells improves production of self-inactivating retroviral vectors. *Gene Ther* 2006; **13**:1524-1533.

44 Tashiro A, Zhao C, Gage FH. Retrovirus-mediated single-cell gene knockout technique in adult newborn neurons in vivo. *Nat Protoc* 2006; **1**:3049-3055.

45 Ory DS, Neugeboren BA, Mulligan RC. A stable human-derived packaging cell line for production of high titer retrovirus/vesicular stomatitis virus G pseudotypes. *Proc Natl Acad Sci U S A* 1996; **93**:11400-11406.

Figure legends

Figure 1 Separation of fluorescence signals emitted by mCherry, Venus and Cerulean into red, green and blue channels by means of two-photon microscopy. (**A**) Emission spectra of the three RGB fluorophores measured in HEK-293 cells expressing one of the three fluorophores. The spectra of mCherry, Venus and Cerulean are plotted in red, green and blue, respectively. Dashed line at 570 nm shows where the dichroic mirror splits emission light. (**B**) Excitation spectra of RGB fluorophores. Venus, mCherry, and Cerulean were expressed separately in HEK-293 cells and the laser power that causes a given fluorescence intensity (fixed at 1400 arbitrary units) of each FP was measured and plotted against the excitation wavelength. Color dots indicate the excitation wavelengths selected for acquisition of fluorescent signals from different FPs in this study. (**C**) Schematic illustration of the findings in (**D**): 800 nm efficiently excites CFP but not Venus, while 990 nm efficiently excites Venus but not CFP. This provides the basis for splitting the fluorescence of the two fluorophores based on their excitation wavelength (see an example in (**D**)). (**D**) *In vivo* maximal intensity projection (MIP) images (54-82 μm, step 2 μm) showing two adult-born JGNs in the same field of view (FOV) expressing Cerulean and Venus, respectively. The red channel is empty (most left image), because there is no cell expressing mCherry in this FOV. The 1st from the right image (RGB) is a merge

of the other three images. Scale bar, 50 μm. (**E**) MIP images (16-68 μm, step 2 μm) illustrating the fluorescent signals from a few RGB marked adult-born JGNs acquired as described in (**D**). Scale bar, 50 μm.

Figure 2 Visualization of the migratory behavior of adult-born neurons by oCPS. (**A**) Schematic drawing of the experimental setup. The mixture of concentrated retroviruses encoding the three fluorescent proteins (Venus as green, mCherry as red and Cerulean as blue) at the ratio of 1:1:1 in terms of infectious titer was injected into the mouse RMS for transduction of adult-born neurons in mice with chronic cranial windows. Transduced cells were imaged every 12 hours starting from DPI 6 by means of two-photon microscopy. (**B**) Left: a MIP image (40-110 μm depth, step 2 μm) of RGB-labeled cells was generated by overlaying three images of basic colors red, green and blue acquired with the pre-determined settings (see Methods). Right: blood vessels were labeled with sulforhodamine B (i.p. injection) and the image of RGB-marked cells (left) was overlaid with blood vessel pattern to get a landmark reference for each cell. (**C**) Upper: schematic drawing illustrating the 7 colors used for marking individual cells in this study. Lower: an example pie chart showing the fraction of adult-born neurons labeled by these colors (out of 111 cells from one of the 6 RGB-marked mice). (**D**) Left: a MIP image (70-120 μm depth, step 2 μm) of an adult-born JGN (arrow) migrating in the GL of the OB. Day 0 is the day of cell's arrival at the GL. Here and in (**E**): asterisks mark previous locations of the cell. Right: plots showing the distance between the two consecutive positions of the cells during their first 12 hours (0-0.5 d) or second 12 hours (0.5-1.0 d) in the GL (Translocation per 12 hours; n=65 cells, 5 mice). Here and in (**E**): medians ± interquartile ranges are shown in red. (**E**) Left: a MIP image (216-336 μm depth, step 2 μm) of an adult-born GC (arrow) migrating in GCL of the OB. Day 0 is the first day when adult-born GC was observed in the GCL. Right: the same graph as in (**D**), but for data obtained

from adult-born GCs (n = 141 cells, 5 mice). Scale bars represent 100 μm in (**B**), (**D**) and (**E**).

Figure 3 Migration angles of adult-born cells in the OB. (**A, B**) An example migration trajectory of an adult-born JGN. The green line indicates the trace in the GL and the red line indicates the trace below the GL or upon entering the GL. GL, glomerular layer; EPL, external plexiform layer; GCL, granule cell layer, MCL, mitral cell layer. MCL is in cyan and the boundary between GL and EPL is in light cyan. The cell was false-colored in grass-green color. Dots represent the cell's positions during consecutive imaging sessions. Scale bar, 100 μm. (**C**) Distributions of mean migration angles (α) of adult-born JGNs as they migrate within the GL or below the GL (including entry steps into the GL), n = 225 cells for Within GL and 92 cells for Below GL, 5 mice. Migration angle is defined as the angle between vertical line and the migration vector in space (see inset). Mean migration angle for each cell is calculated based on all the migration steps of the cell within the given layer. (**D**) Paired comparison of mean migration angles of the individual JGNs Below and Within the GL (n=92 cells, 5 mice). Each data point represents one cell with complete migration history. The dashed line is the unity (x = y) line. (**E**) An example migration trajectory of an adult-born GC. (**F**) Distribution of mean migration angles of adult-born GCs migrating in the GCL (n=144 cells, 5 mice). (**G**) Box plot comparing mean migration angles of JGNs in GL and GCs in GCL (values are shown as median ± interquartile range; n=225 JGNs, 144 GCs from 5 mice; ***P<0.001, Mann-Whitney test).

Figure 4 Temporal migration pattern of adult-born JGNs. (**A**) Migration speed (Translocation per 12 hours) of an example adult-born JGN plotted against time (DPI). Note the stop-and-go behavior of the cell. (**B**) 2D plot of the migration speed for adult-born JGNs, which settled down within the FOVs (n=62 cells, 5 mice), on different days

before their settlement. Arrows point to the high speed phase of a few JGNs. (**C**) False colored single frame images of an adult-born JGN and surrounding blood vessels (DPI 8, 30 µm below the dura) taken at different time points as indicated (see timestamp, relative time). Scale bar, 20 µm. (**D**) Distance traversed by the cell shown in (**C**) during consecutive 15-min-long time intervals plotted as a function of time. (**E, F**) 2D plots of the migration speed (translocation per 15 min) of adult-born JGNs on DPI 8 (**E**, n = 17 cells, 5 mice) and on DPI 14 (**F**, n = 18 cells, 4 mice). (**G, H**) Box plots showing the median migration speed (**G**) and maximum migration speed (**H**) of cells sown in (**E, F**). Median migration speed was significantly different between the two age groups (Mann-Whitney test, $^{**}P \leq 0.01$). No significant difference was found between the two groups in terms of maximum migration speed ($P=0.1$). (**I**) Box plot showing the maximum duration of a stationary period during the period of 4 hours. No significant difference was found between DPI 8 and DPI 14 (Mann-Whitney test, $P=0.8$). (**J**) Box plot showing the cumulative stationary period for each cell during the 4-hour-long observation time window. No significant difference was found between DPI 8 and DPI 14 (Mann-Whitney test, $P=0.2$). In (**G-J**), all values are shown as median ± interquartile range. Data shown in (**E-J**) belong to the same dataset.

Figure 5 Spatial migration pattern of adult-born JGNs. (**A**) Migration history of 10 JGNs in an example FOV (top view). Each trace is shown in a different color. Scale bar, 50 µm. (**B**) Examples of two different types of migration trajectories of adult-born JGNs. Upper: unidirectional migration, the maximal migration angle (θ) between the two immediately adjacent migration steps is ≤ 90º. Lower: multidirectional migration, θ > 90º. Scale bar, 100 µm. (**C**) Fraction of uni- or multidirectionally migrating cells (n=5 mice, 15-69 cells per mouse). Solid lines connect the data obtained in the same animal. (**D**) Comparison of net migration distance (distance between the entry sites into the GL and the final cell's

position) between uni- and multidirectional JGNs (n=93 and 120 cells, respectively, 5 mice). No significant difference was found by Mann-Whitney test (P=0.99). (**E**) Comparison of total migration distance (the cumulative distance traveled in GL) between uni- and multidirectional cells (n=93 and 120 cells, respectively, 5 mice). Significantly longer cumulative distances were found for cells with multidirectional migration; ***P<0.001, Mann-Whitney test. All values are shown as median ± interquartile range.

Figure 6 Adult-born neurons show different migration speed across layers of the OB. (**A**) Comparison of median migration speed of the same JGNs in different layers of the OB. Paired data were obtained from the same cells migrating Within GCL, Through EPL (between MCL and GL) or Within GL (n=43 cells with recorded trace inside GCL, 4 mice, *P<0.05, ***P<0.001, Kruskal-Wallis test followed by Dunn's multiple comparison test). Here and in (**B**) for cells, which made more than one migration step within the layer, the entries represent the mean values. (**B**) Comparison of mean migration angles measured as cells migrated through different layers of the OB. Same data set as in (**A**); ***P<0.001, Kruskal-Wallis test followed by Dunn's multiple comparison test. (**C**) 2D plots of the migration speed (Translocation per 12 hours) of JGNs and GCs in the GCL on different days before settlement (for GCs) or before leaving GCL (n=43 JGNs, 4 mice, and 103 GCs, 5 mice). (**D**) Comparison of migration speed of JGNs and GCs on different time points before exiting GCL (for JGNs) or settlement (for GCs). Same data set as in (**C**); P=0.3 (Mann-Whitney test) for comparison between the JGNs and GCs on 1.5-1.0 d; P=0.1 on 1.0-0.5 d and ***P<0.001 on 0.5-0 d. (**E**) Migration angles of JGNs and GCs in GCL; P=1.0, Mann-Whitney test; for JGNs, n=43 from 4 mice; for GCs, n=144 from 5 mice. Values are shown as median ± interquartile range.

Figure 7 Motility of adult-born cells gradually decreases with time spent in the destination layer. (**A**) Upper: overlay of adult-born JGN positions recorded at DPI 9 and DPI 10 (left), as well as at DPI 28 and DPI 30 (right). MIP images from 30-110 μm, step 2 μm. Lower: a graph showing the fractions of moving cells at different DPIs. (**B**) Similar data as in (**A**) but obtained for adult-born GCs. MIP images from 260-360 μm, step 2 μm. Scale bar, 100 μm. (**C**) The fraction of stable cells plotted as the function of time (DPI). Median with one interquartile range is shown on each time point (n=6 FOVs from 4 mice for GCs and n=11 FOVs from 4 mice for JGNs). (**D**) Box plot illustrates the day when accumulation of 90% of the stable population is achieved. All values are shown as median ± interquartile range. Same data set as (**C**), $^{**}P<0.01$, Mann-Whitney test. (**E**) Paired comparison of the first and the last migration steps of individual adult-born JGNs (n=32 cells, 5 mice) and GCs (n=48 cells, 5 mice) in their destination layers; $^{***}P<0.001$, Wilcoxon matched pairs test. The median size of the first and the last step was also compared between JGNs and GCs. Mann Whitney test, $P=0.9$ and 0.8, respectively.

Figure 8 An updated model of adult-born cell migration in the olfactory bulb. Previously adult-born cells within the bulb were thought to undergo radial migration only (yellow arrows). The migration speed was unknown and therefore assumed to be homogenous. In this study, we found that pure radial migration is seen only for adult-born granule cells (GCs). Adult-born JGNs first migrate radially together with GCs in GCL (red arrows for GCs, green arrows for JGNs). Whereas GCs slow down to integrate into the GCL, the JGNs speed up to quickly traverse EPL. When reaching the GL adult-born JGNs switch to lateral migration, moving either uni- or multi-directionally. They gradually slow down, integrating some 1-2 glomeruli away from their initial entry site.

Figure 1 Separation of fluorescence signals emitted by mCherry, Venus and Cerulean into red, green and blue channels by means of two-photon microscopy

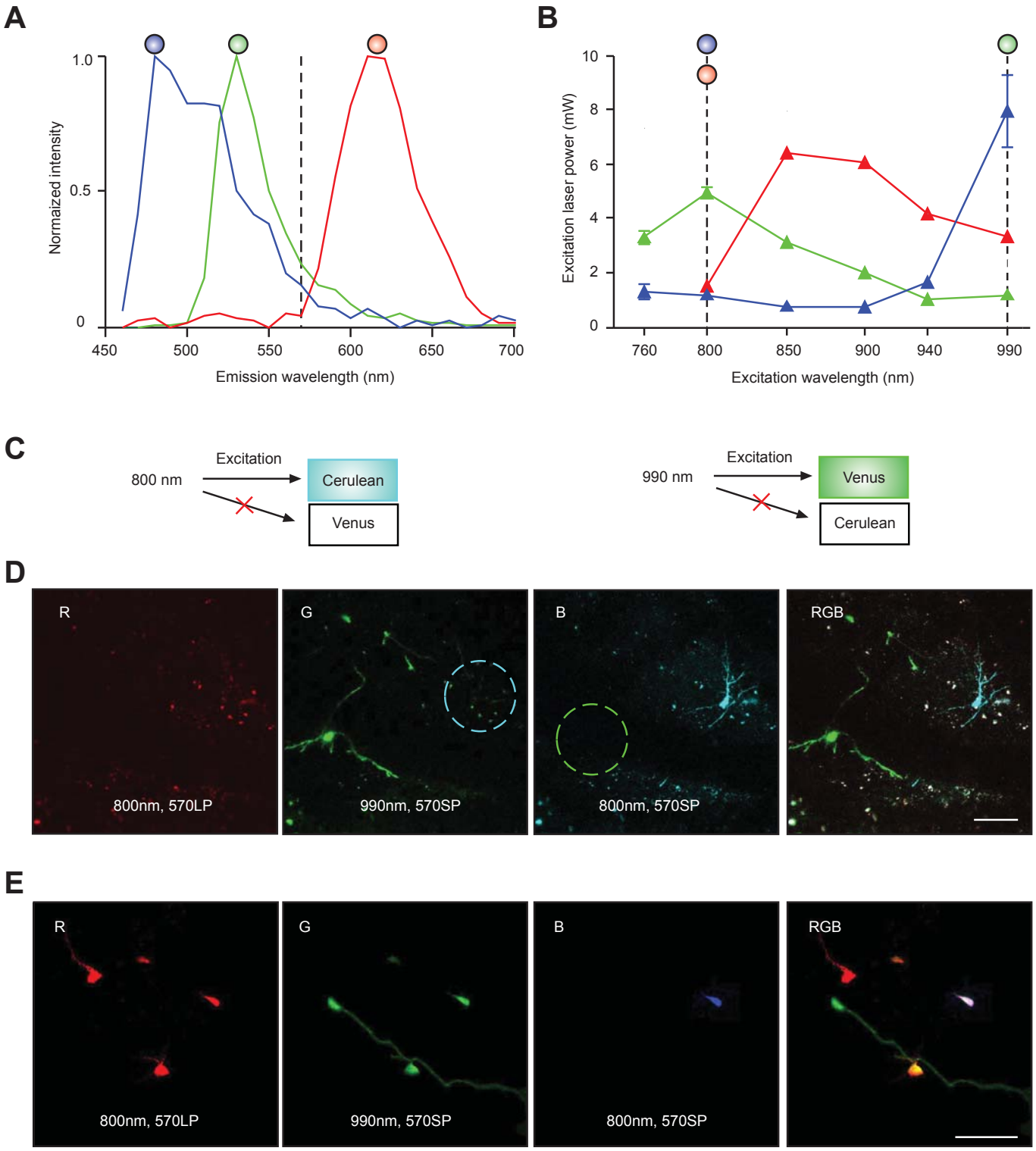

Figure 2 Visualization of the migratory behavior of adult-born neurons by oCPS

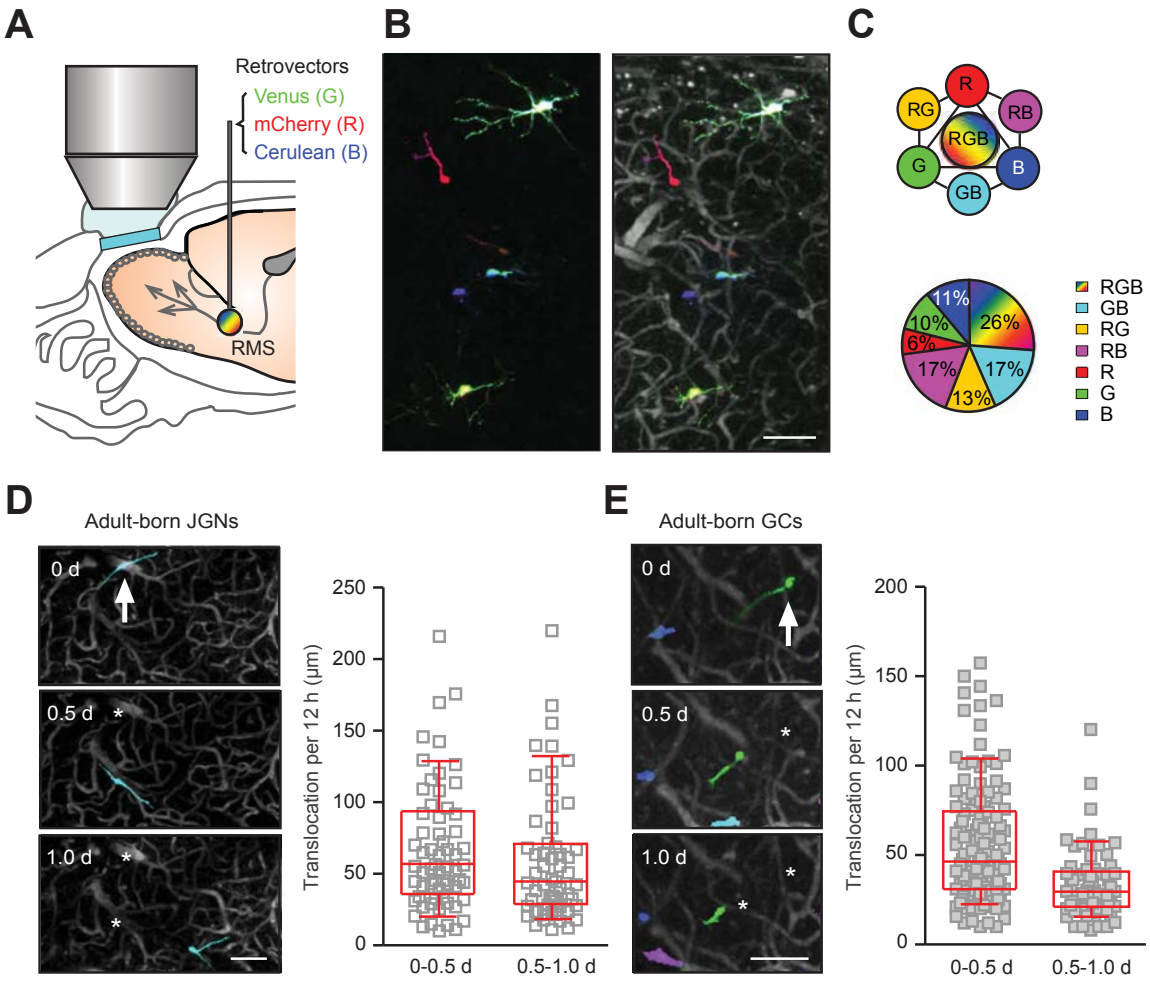

Figure 3 Migration angles of adult-born cells in the olfactory bulb

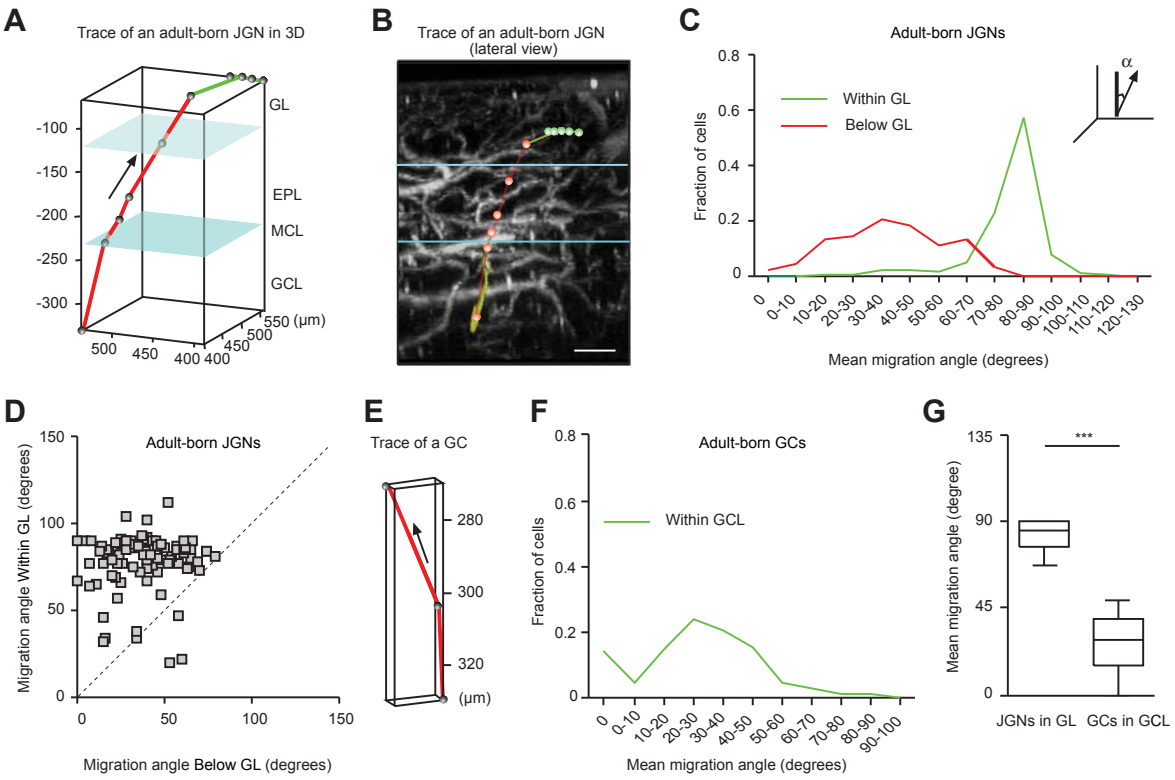

Figure 4 Temporal migration pattern of adult-born JGNs

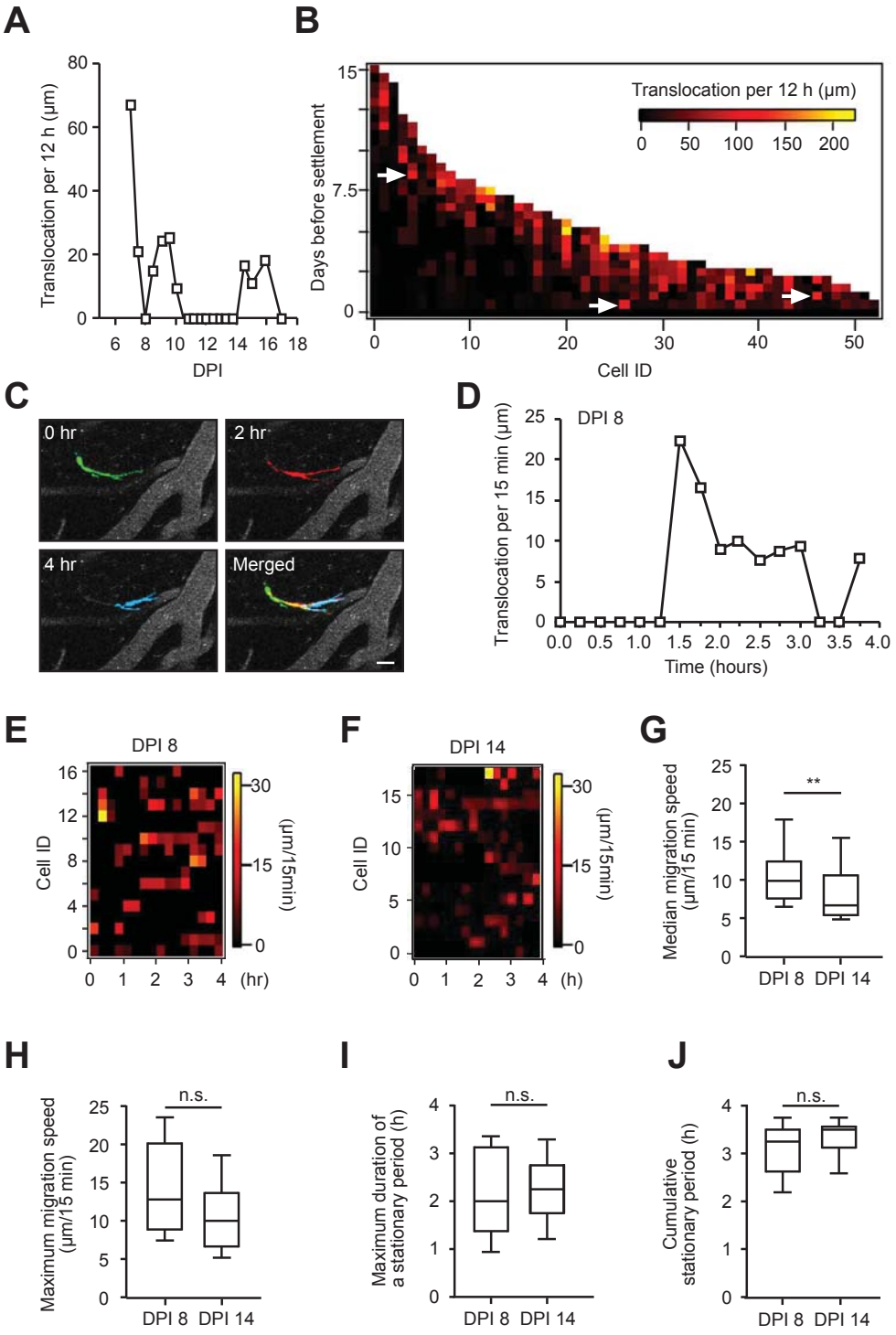

Figure 5 Spatial migration pattern of adult-born JGNs

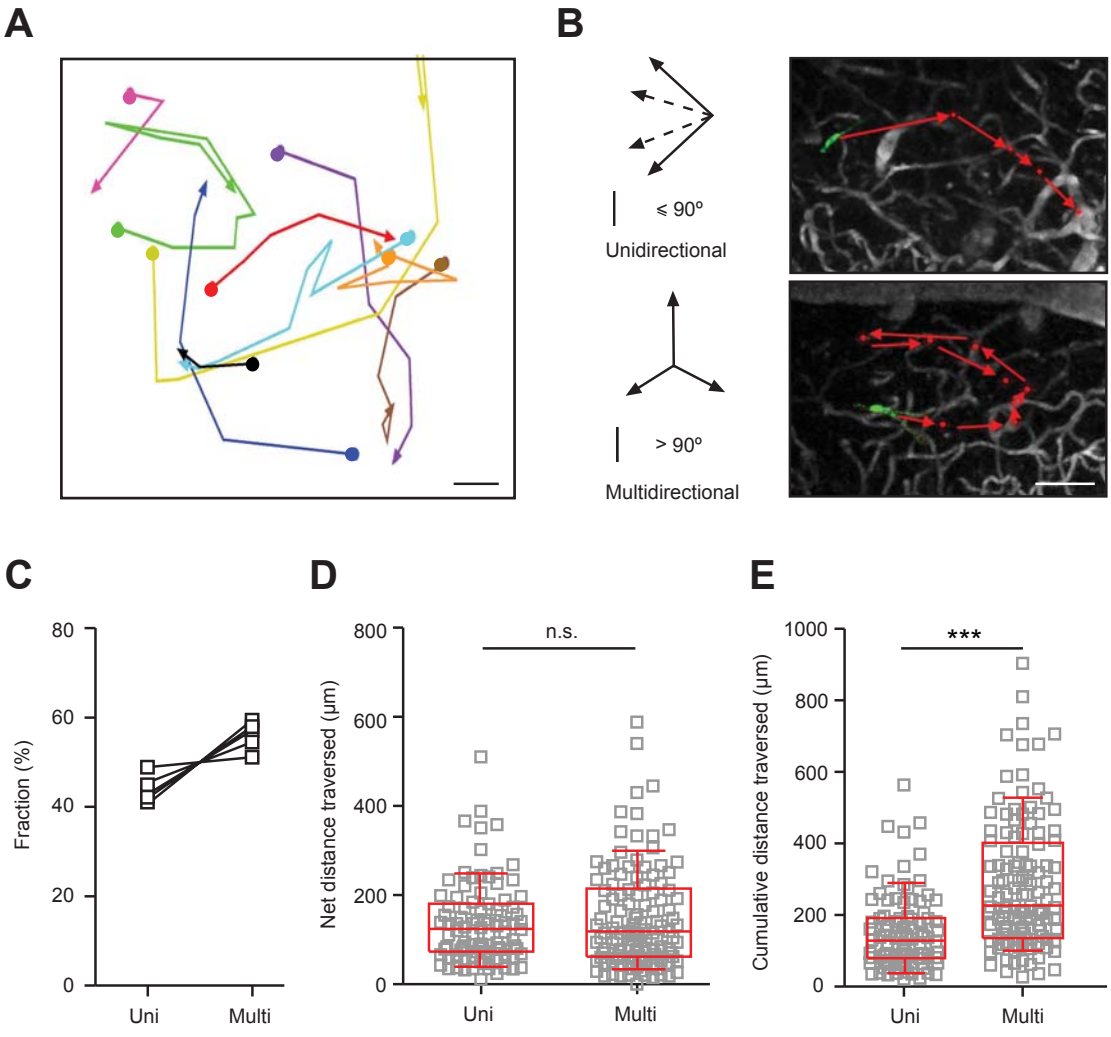

Figure 6 Adult-born neurons show differential migration speed across layers of the olfactory bulb

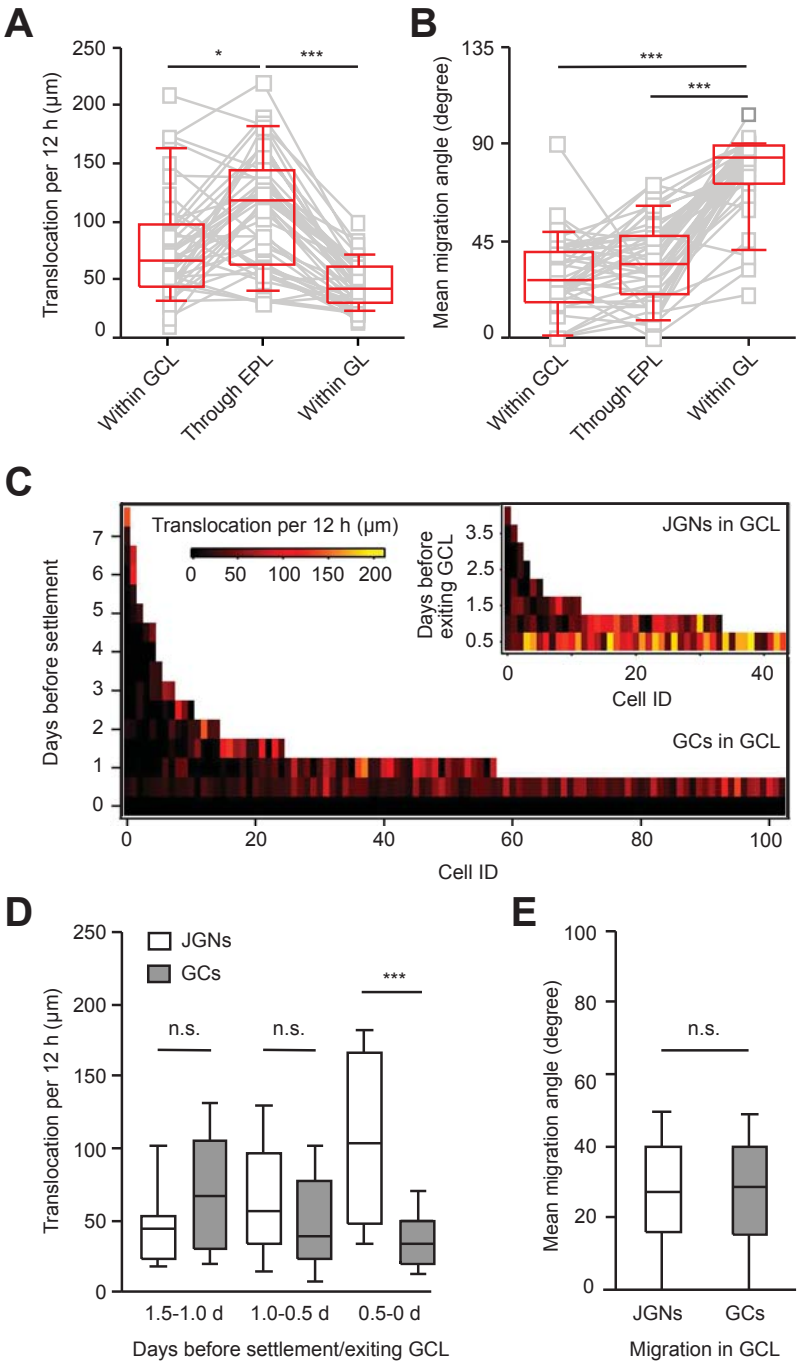

Figure 7 Motility of adult-born cells gradually decreases with time spent in the destination layer

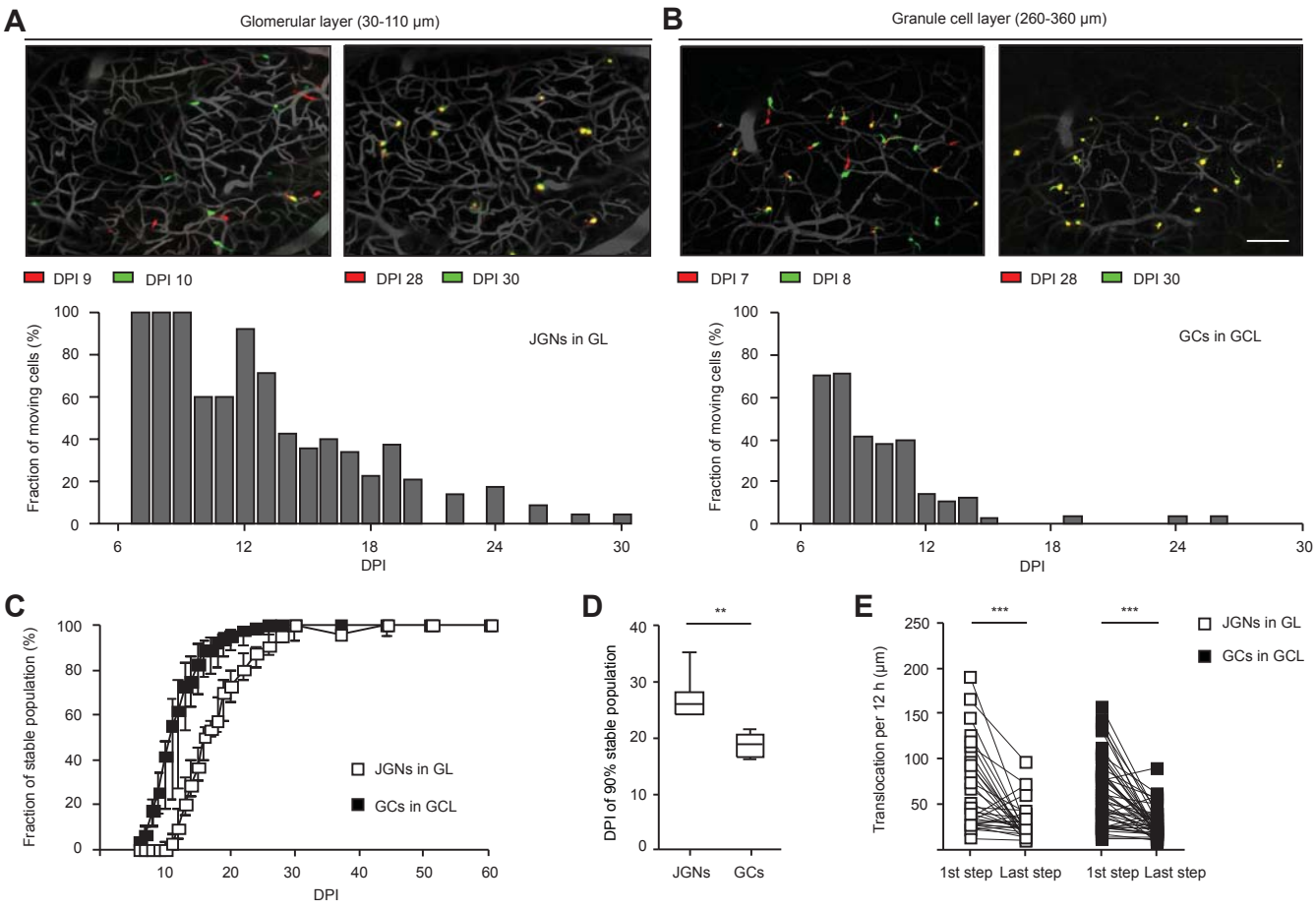

Figure 8 An updated model of adult-born cell migration in the olfactory bulb